GOES-R Advanced Baseline Imager: spectral response functions and radiometric biases with the NPP Visible Infrared Imaging Radiometer Suite evaluated for desert calibration sites

Aaron Pearlman,[1,*] David Pogorzala,[2] and Changyong Cao[3]

[1]Earth Resources Technology, Inc., 14401 Sweitzer Lane Suite 300, Laurel, Maryland 20707, USA

[2]Integrity Applications Incorporated, 15020 Conference Center Drive, Suite 100, Chantilly, Virginia 20151, USA

[3]NOAA/NESDIS/STAR, 5825 University Research Court, Suite 3250, College Park, Maryland 20740, USA

*Corresponding author: aaron.pearlman@ertcorp.com

Received 17 June 2013; revised 2 October 2013; accepted 6 October 2013;
posted 7 October 2013 (Doc. ID 192352); published 31 October 2013

The Advanced Baseline Imager (ABI), which will be launched in late 2015 on the National Oceanic and Atmospheric Administration's Geostationary Operational Environmental Satellite R-series satellite, will be evaluated in terms of its data quality postlaunch through comparisons with other satellite sensors such as the recently launched Visible Infrared Imaging Radiometer Suite (VIIRS) aboard the Suomi National Polar-orbiting Partnership satellite. The ABI has completed much of its prelaunch characterization and its developers have generated and released its channel spectral response functions (response versus wavelength). Using these responses and constraining a radiative transfer model with ground reflectance, aerosol, and water vapor measurements, we simulate observed top of atmosphere (TOA) reflectances for analogous visible and near infrared channels of the VIIRS and ABI sensors at the Sonoran Desert and White Sands National Monument sites and calculate the radiometric biases and their uncertainties. We also calculate sensor TOA reflectances using aircraft hyperspectral data from the Airborne Visible/Infrared Imaging Spectrometer to validate the uncertainties in several of the ABI and VIIRS channels and discuss the potential for validating the others. Once on-orbit, calibration scientists can use these biases to ensure ABI data quality and consistency to support the numerical weather prediction community and other data users. They can also use the results for ABI or VIIRS anomaly detection and resolution. © 2013 Optical Society of America

OCIS codes: (280.4788) Optical sensing and sensors; (010.0280) Remote sensing and sensors; (010.5620) Radiative transfer; (110.4234) Multispectral and hyperspectral imaging.

http://dx.doi.org/10.1364/AO.52.007660

1. Introduction

The National Oceanic and Atmospheric Administration maintains both polar and geostationary operational Earth-observing platforms that together enable full coverage of the earth. The newest geostationary satellite, the Geostationary Operational Environmental Satellite R-series (GOES-R), slated to launch in late 2015, will mark the beginning of the new generation of GOES satellites carrying the Advanced Baseline Imager (ABI). The ABI is designed to have significantly improved spectral, spatial, and temporal resolution and upgraded navigation and registration accuracy compared with the imagers currently providing operational coverage onboard GOES 13 and 15 [1,2]. It will enhance the capabilities of forecasters and scientists to predict weather events and monitor climate and the environment.

1559-128X/13/317660-09$15.00/0
© 2013 Optical Society of America

The increased spectral coverage, for instance, will provide an increased understanding of the role of aerosols in weather and climate, particularly in the visible and near infrared (VNIR) channels. Compared with the six spectral channels on the current imagers, only one of which is in the visible and none in the near infrared, the ABI will have 16 spectral channels: two in the visible and four in the near infrared wavelength range. In addition, the ABI will house an on-board sub-aperture solar diffuser to enable operational calibration updates for these channels, a new feature for GOES imagers, resulting in lower uncertainty in products such as aerosol optical depth and aerosol detection [3–5].

Operators and scientists also maintain product quality on-orbit by comparing responses of current sensors that have similar spectral channels. They often use the simultaneous nadir overpass (SNO) method, which, because of its low uncertainty, can show biases resulting from sensor physics—on-orbit calibration, detector nonlinearity, noise performance, and spectral response knowledge—and not introduced by the method itself [6,7]. The knowledge of the spectral response functions (or response versus wavelength) of the channels often dominates this uncertainty; therefore, to decrease its impact in future comparisons, the designers of the ABI spectral channels chose them to match current imagers, such as the Moderate Resolution Imaging Spectrometer (MODIS) aboard Aqua and Terra satellites and the Visible Infrared Imaging Radiometer Suite (VIIRS) aboard the Suomi National Polar-orbiting Partnership satellite. Also, by having matching channels, both sensors can observe phenomenology with similar algorithms, which is helpful for validating weather products. VIIRS has channels near the 0.47, 0.64, 0.86, 1.38, 1.61, and 2.25 μm center wavelengths that match the ABI VNIR channels, also called reflective solar bands, and other matching ones in the thermal infrared range.

VIIRS, which was launched in October of 2011, continues the Polar Orbiting Environmental Satellite (POES) program and has, so far, produced high-quality data during its post-launch testing phase [8,9]. To reduce uncertainties from knowledge of the spectral responses, the sensor was characterized prelaunch and validated using the National Institute of Standards and Technology Spectral Irradiance and Radiance Responsivity Calibrations using Uniform Sources (SIRCUS) for VNIR channels [10]. Calibration scientists have traced radiometric biases, using SNO comparisons between it and MODIS, to differences in their spectral response functions [8].

Likewise, the instrument developers for ABI had to derive accurate spectral response functions (recently released) so that potential radiometric biases could be resolved. These spectral responses for each channel include the effects of all optical elements such as mirrors, beamsplitters, windows, bandpass filters, and optical detectors (Fig. 1). The instrument developer measured each part's transmittance/reflectance spectrum or quantum efficiency (for the detectors) and multiplied them together to obtain the system spectral response for each channel, which included both the in-band and out-of-band responses.

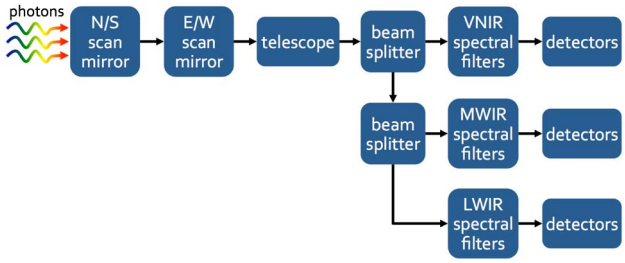

Fig. 1. Basic optical layout of ABI (N/S, north/south; E/W, east/west; MWIR, mid-wave infrared; LWIR, long-wave infrared). The spectral response function for each channel accounts for the effects of all optical components and detectors in its path.

Spectral response functions were validated through additional bandpass filter transmittance measurements and system-level spectral measurements with SIRCUS. National Institute of Standards and Technology (NIST) personnel measured the bandpass filter spectral transmittances since these dominate the spectral response functions [11]. They measured filters similar to (and produced in the same coating run as) those installed in the ABI, with the same angles of incident radiation and temperatures, as if installed and operated on the ABI. This reduced spectral response uncertainties associated with known effects of interference filters related to their temperatures and angles of incidence. SIRCUS validated the vendor's ability to derive the total response from the effects of individual optical elements and detectors in most of the VNIR channels.

Even though the ABI spectral responses roughly match VIIRS, their differences will produce radiometric biases when comparing them on-orbit. Scientists have predicted responses and biases between satellite sensors for other instruments by applying spectral response functions to simulated at-sensor spectral radiances or top-of-atmosphere reflectances using both radiative transfer simulations and also hyperspectral aircraft/satellite sensor measurements [12–15]. These simulations and aircraft campaigns assume or view well-characterized Earth targets with spatially and temporally uniform optical properties, such as deserts [16–19]. Bremer *et al.* have also discussed the importance of matching spectral bands between VIIRS and ABI and on-orbit opportunities for their cross-calibration [3].

We now have the opportunity to study the recently released ABI spectral response functions and compare them with VIIRS to maintain consistency between polar and geostationary instrument data for the numerical weather prediction community, using similar techniques to those mentioned above. The radiometric biases between ABI and VIIRS are predicted by computing their responses to earth scenes at well-characterized desert sites: the Sonoran Desert and White Sands National Monument [17,18],

and then quantifying the uncertainties of these values. We validate these uncertainties in several channels using aircraft hyperspectral sensor data and discuss the potential for validating other channels by incorporating other sources of uncertainty in the analysis. Once both sensors are on-orbit, calibration scientists can also use the predictions (modified for view angle effects) in the validated channels to judge whether the differences between the sensors can be attributed to their expected uncertainties or to a sensor problem. Subsequent flight campaigns, based on these results, could validate all channels for these instruments.

2. Methods

A. Data

We used ground target reflectance, aerosol, and water vapor measurments of sites near the Sonoran Desert (Fig. 2), located in the Mexican state of Sonora, near the United States–Mexico border, and White Sands National Monument, located in southern New Mexico. Ground target material samples taken near the sites were measured in a laboratory with a tungsten lamp, white panel reference, and a spectroradiometer to obtain their spectral reflectances. The Sonoran Desert samples were measured and then roughened to simulate wind-roughened sand dunes and measured again. White Sands samples were measured before and after mixing and with their surfaces roughened. We computed the mean (Fig. 3) and standard deviation across all conditions for each site and, from the following, obtained water vapor and aerosol optical depth data: the Aerosol Robotic Network (AERONET) at White Sands, and a handheld sun photometer near the Sonoran Desert [20,21].

The Airborne Visible/Infrared Imaging Spectrometer (AVIRIS), aboard NASA's ER-2 jet, provided spectral radiance data in the 400–2500 nm wavelength range, with 10 nm sampling and spectral resolution [22], over both the Sonoran Desert and White Sands National Monument. Figure 2 shows the locations of the collected target samples, sun photometer measurements, and a true color composite of the AVIRIS radiance imagery. The footprint (defined here as the pixel ground instantaneous field of view) over White Sands and the Sonoran sites were 15.7 m × 15.7 m and 16.3 m × 16.3 m, respectively. The ABI/VIIRS footprint is defined in the next section.

The spectral response functions for both ABI and VIIRS are publicly available [23,24].

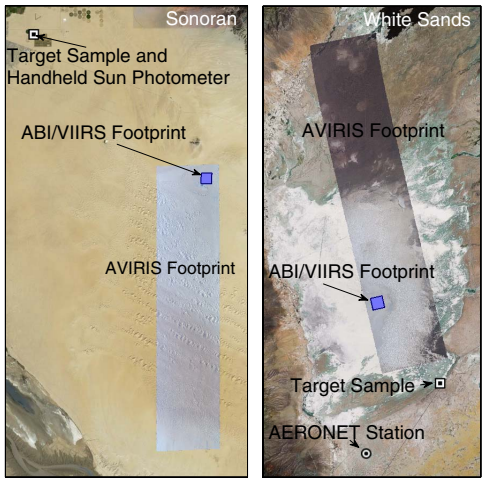

Fig. 2. Locations of sample collections, sun photometer measurements (handheld or AERONET), AVIRIS true color composite (using 462.8, 550.3, 638.2 nm wavelength bands), and ABI/VIIRS footprint chosen for the Sonoran Desert (left) and White Sands (right) sites. Note that the ABI and VIIRS footprints assume the same size for our simplified case.

B. Radiometric Biases

For analogous reflective solar bands of VIIRS and ABI, shown in Fig. 3 and referred to as M3/047, I1/064, M7/086, M9/138, M10/161, and M11/225 for VIIRS/ABI channels, we determined the TOA reflectances of ABI and VIIRS and their uncertainties using two methods: radiative transfer simulations (constrained by ground measurements) and aircraft measurements. The difference between the ABI and VIIRS TOA reflectance for a given pair of analogous channels is defined as the radiometric bias. The ratio between ABI and VIIRS TOA reflectances are spectral band adjustment factors and can be used for converting measured VIIRS (ABI) effective TOA reflectances to ABI (VIIRS) values [12].

The water vapor, aerosol, and surface reflectance data, assuming a Lambertian surface, and the view geometry and atmospheric conditions of the AVIRIS measurements constrained our radiative transfer

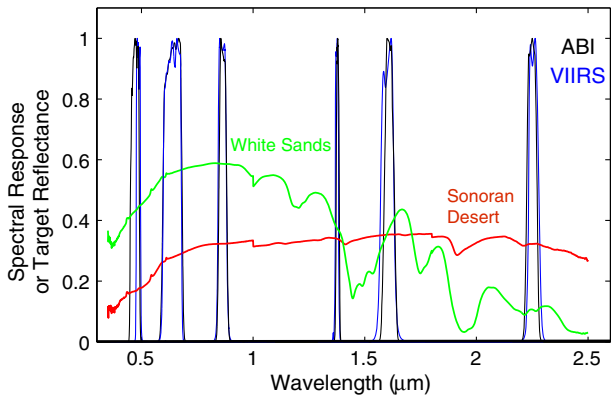

ABI Channels	VIIRS Channels	Spatial Resolution ABI (km)	VIIRS (km)	Sample Use
047	M3	1.0	0.75	Aerosols
064	I1	0.50	0.38	Aerosols/Clouds
086	M7	1.0	0.75	Aerosols
138	M9	2.0	0.75	Cirrus Clouds
161	M10	1.0	0.75	Snow
225	M11	2.0	0.75	Clouds

Fig. 3. (Top) analogous ABI and Visible Infrared Radiometer Imaging Suite (VIIRS) spectral response functions and spectral reflectance of sand samples taken near White Sands missile range and the Sonoran Desert. (Bottom) Channels names, spatial resolution at nadir, and sample use. Note that ABI channels are labelled according to their nominal central wavelengths (for instance, 047 = 0.47 μm).

Table 1. Parameters for Radiative Transfer Simulations

Parameter	Sonoran Desert	White Sands
Date	June 10, 2011	May 23, 2011
Solar zenith (deg)	45.1	45.3
Solar azimuth (deg)	89.0	93.0
Atmosphere	Mid-latitude summer	Mid-latitude summer
Water vapor (g/cm^2)	1.44	0.47
Ozone (cm-atm)	0.319	0.319
Aerosol	desert model	desert model
Aerosol optical depth, 550 nm	0.0606	0.133
Sensor level (km)	19.4	19.3

calculations generated with 6SV and MODTRAN radiative transfer codes (Table 1) [25–27]. 6SV generates spectral TOA reflectance with 2.5 nm resolution and MODTRAN generates spectral radiance with 1 nm resolution for our simulations. The ABI and VIIRS spectral response functions ($\phi_{i,j}(\lambda)$) were resampled to the wavelengths of the outputs, where ABI and VIIRS are represented by $i = 1$ and 2, respectively, and the channels by j. We then converted the MODTRAN spectral radiance outputs to TOA spectral reflectance with $\rho_\lambda = (\pi L_\lambda d^2)/(E_{\text{solar}} \cos(\theta))$, where L_λ is spectral radiance, d is the Earth–Sun distance divided by the mean Earth–Sun distance, and θ and E_{solar} is the solar zenith angle and solar irradiance given by the Thuillier (2002) Model [28], respectively, and computed the TOA reflectance effective values:

$$\rho_{i,j} = \frac{\int \rho(\lambda)\phi_{i,j}(\lambda)\mathrm{d}\lambda}{\int \phi_{i,j}(\lambda)\mathrm{d}\lambda}. \tag{1}$$

The radiometric bias is the difference between the VIIRS and ABI effective TOA reflectance values ($\rho_{2,j} - \rho_{1,j}$).

Hyperspectral data from AVIRIS can be used to find radiometric biases without radiative transfer simulations. However, these data introduce other complications, since AVIRIS has a different footprint than ABI or VIIRS and coarser spectral resolution than the spectral responses of ABI or VIIRS channels. The footprints of ABI and VIIRS will depend on the on-orbit geometry, so we accounted for the differences in footprints between AVIRIS and ABI/VIIRS by taking a simplified case: combining pixels over the nadir footprint of the lowest resolution ABI channel (2 km × 2 km at nadir) (Fig. 2). In one example, however, we found the bias for a slightly more realistic case using the nadir footprint of VIIRS (375 m or 750 m) and ABI for each channel (500 m, 1 km, or 2 km). The regions were chosen by their maximum spatial uniformity and computed by taking the minimum relative standard deviation over the AVIRIS channels that correspond to ABI channels, calculating the mean spectral radiance in that region, interpolating with a cubic spline to the ABI or VIIRS channel wavelength resolution, converting to effective TOA reflectance over the ABI and VIIRS channels, and calculating the bias. In an attempt to determine the best match between MODTRAN-simulated and AVIRIS image radiances, we repeated the analysis on the mean of a selection of image pixels found with the spectral angle mapper algorithm [29]. The algorithm was used to select pixels with a spectral angle less than 0.06 radians from the MODTRAN-simulated spectral radiance.

C. Uncertainty Analysis

Adhering to the international guidelines for numerical calculations given in the Guide to the Expression of Uncertainty in Measurement (GUM) [30], we derived the combined uncertainties of the simulated TOA reflectances [$u_c(\rho)$] using the instrument measurement and input parameter uncertainties, where l and m represent any pair of measurement or parameter inputs:

$$u_c(\rho) = \sqrt{\sum_{l=1}^{N}\sum_{m=1}^{N} Z_l Z_m r(x_l, x_m)}, \tag{2}$$

where

$$Z_l = \frac{1}{2}[\rho(x_l + u(x_l)) - \rho(x_l - u(x_l))]$$
$$Z_m = \frac{1}{2}[\rho(x_m + u(x_m)) - \rho(x_m - u(x_m))]. \tag{3}$$

$r(x_l, x_m)$ is the correlation coefficient between inputs to account for the contribution of correlated input parameters to the uncertainty. The expressions in Eq. (3) show input parameters, with their added and subtracted uncertainties $x \pm u(x)$, contribute to the uncertainty in reflectance (found via 6SV) $\rho(x \pm u(x))$, for that input Z (where the subscripts are dropped for brevity). The contributions are summed over all inputs. The equation is a version of the propagation of uncertainties formula adapted for numerical calculations [30].

We considered the TOA reflectance uncertainties due to the measured water vapor and AOD using their reported uncertainties and accounted for their correlation by calculating r (= −0.05 and −0.06 for White Sands and Sonoran Desert sites, respectively) and data taken from repeated measurements at both sites [21]. For the sample sand reflectance, we only considered the uncertainty due to variation in the measured reflectance from different samples and surface conditions.

In this study, radiometric requirements represent the instrument measurement uncertainty, which includes all uncertainties in the knowledge of the spectral response functions. The product measurement requirements in ABI documentation use the terms accuracy, and short- and long-term repeatability, instead of uncertainty, so we translate them to uncertainty using a procedure that will be the subject of a future paper and outlined here [30–32]: We decide on

the probability distribution that corresponds to each requirement; for short term repeatability, the Gaussian distribution is used because it describes the dispersion of results from repeated measurements. We interpret accuracy as bias and use a rectangular distribution, applying a rectangular distribution for the long-term drift requirement. The half-width of the rectangular distributions (δ, b for accuracy and long-term drift, respectively), and the standard deviation of the Gaussian (s), represent their standard uncertainties. The three sources of uncertainty combine according to the propagation of the uncertainties formula for independent inputs (also called the root sum of squares formula): $\delta = 5\%$, $b = 1.5\%$, and $s = 0.2\%$ [33]. This gives a combined uncertainty of 3.02% ($k = 1$) in spectral radiance, as described by Eq. (4)

$$u(x) = \sqrt{s^2 + \frac{\delta^2}{3} + \frac{b^2}{3}}. \tag{4}$$

Requirements for VIIRS express uncertainty in terms of TOA reflectance (of 2%, $k = 1$), so the ABI instrument uncertainty was propagated in the conversion from radiance to TOA reflectance [34]. TOA reflectance uncertainties were found by combining the inputs and instrument contributions (via the root sum of squares formula) and the uncertainty of the radiometric bias was found by combining the ABI and VIIRS TOA reflectance uncertainties with the ABI and VIIRS instrument uncertainties.

We performed a similar uncertainty analysis of effective ABI/VIIRS TOA reflectances derived from AVIRIS measurements. The atmospheric effects above the aircraft, such as ozone absorption, were omitted to remain consistent with our original simulations and generating the reflectance values at aircraft altitude. To account for the interpolation uncertainty, we followed Ref. [35] and found that the uncertainties of interpolated values were less than and within a few percent of the uncertainty of the original spectral radiance data. This finding is consistent with the results in Ref. [35] in that the uncertainty can remain below the uncertainty of the input data using cubic spline interpolation. So the original quoted uncertainty of 4% in spectral radiance remains largely unchanged from interpolation and was kept as a conservative estimate for each interpolated AVIRIS data point. These points were propagated to effective ABI/VIIRS channel TOA reflectances to determine their uncertainties [22].

3. Results and Discussion

Table 2 shows the 6SV radiative transfer simulation results in terms of TOA reflectances, VIIRS-ABI bias, and bias uncertainty over the Sonoran Desert and White Sands sites. The small magnitude of these biases shows that the ABI and VIIRS channels match closely. The two types of desert targets affect the bias with White Sands having a larger bias magnitude than the Sonoran target in most of the channels. The bias between M10 and 161 for White Sands is the largest among the channels, since the responses are spectrally shifted with respect to each other over a sensitive portion of the target spectrum, as shown in Fig. 3. Other significant biases are shown between M3 and 047 and between M9 and 138 due to significant shifts and/or differences in spectral widths and high target sensitivity. Also note that the uncertainties are much larger than the biases in all cases.

The uncertainty components shown in Fig. 4 reveal that the largest uncertainties in the VIIRS and ABI TOA reflectances are the instrument uncertainty, including all calibration, spectral response, and measurement uncertainty inherent to the instrument, and the target reflectance uncertainty. The instrument uncertainty is higher for ABI than VIIRS because of VIIRS' stricter requirements. The negligible water vapor and aerosol optical depth contributions reflect the well-calibrated ground equipment and low sensitivity of these inputs to the TOA reflectance. One exception is the high uncertainty for M9 at White Sands to water vapor because of its position within an atmospheric water vapor absorption band. Since the water vapor and aerosol optical depth were generally small, we left out the even smaller contribution introduced by the correlation between them. The uncertainties in reflectance units were 0.04–0.05 and 0.04–0.08 for the Sonoran Desert and White Sands sites, respectively, using radiative transfer code and measured reflectance spectra, aerosol optical depth, and water vapor (Fig. 4).

Using AVIRIS images, we validated the TOA reflectances in two ABI and two VIIRS channels for

Table 2. Spectral Radiometric Biases in TOA Reflectance for Sonoran Desert and White Sands using 6SV

	VIIRS/ABI Channels->	M3/047	I1/064	M7/086	M9/138	M10/161	M11/225
Sonoran Desert	VIIRS TOA reflectance	0.200	0.265	0.318	0.00394	0.338	0.293
	ABI TOA reflectance	0.201	0.265	0.319	0.00422	0.339	0.297
	Bias (6SV)	**−0.0011**	**-1.2×10^{-5}**	**-5.8×10^{-4}**	**-2.8×10^{-4}**	**−0.0012**	**−0.0037**
	Uncertainty of bias[a] ($k = 1$)	**0.042**	**0.047**	**0.050**	**0.044**	**0.049**	**0.050**
White Sands	VIIRS TOA reflectance	0.437	0.526	0.586	0.0324	0.345	0.0955
	ABI TOA reflectance	0.429	0.526	0.586	0.0339	0.359	0.0952
	Bias (6SV)	**0.0085**	**-5.8×10^{-6}**	**-2.2×10^{-4}**	**−0.0015**	**−0.014**	**3.0×10^{-4}**
	Uncertainty of bias[a] ($k = 1$)	**0.051**	**0.064**	**0.075**	**0.038**	**0.059**	**0.039**

[a] k is the coverage factor, where $k = 1$ represents the standard uncertainty.

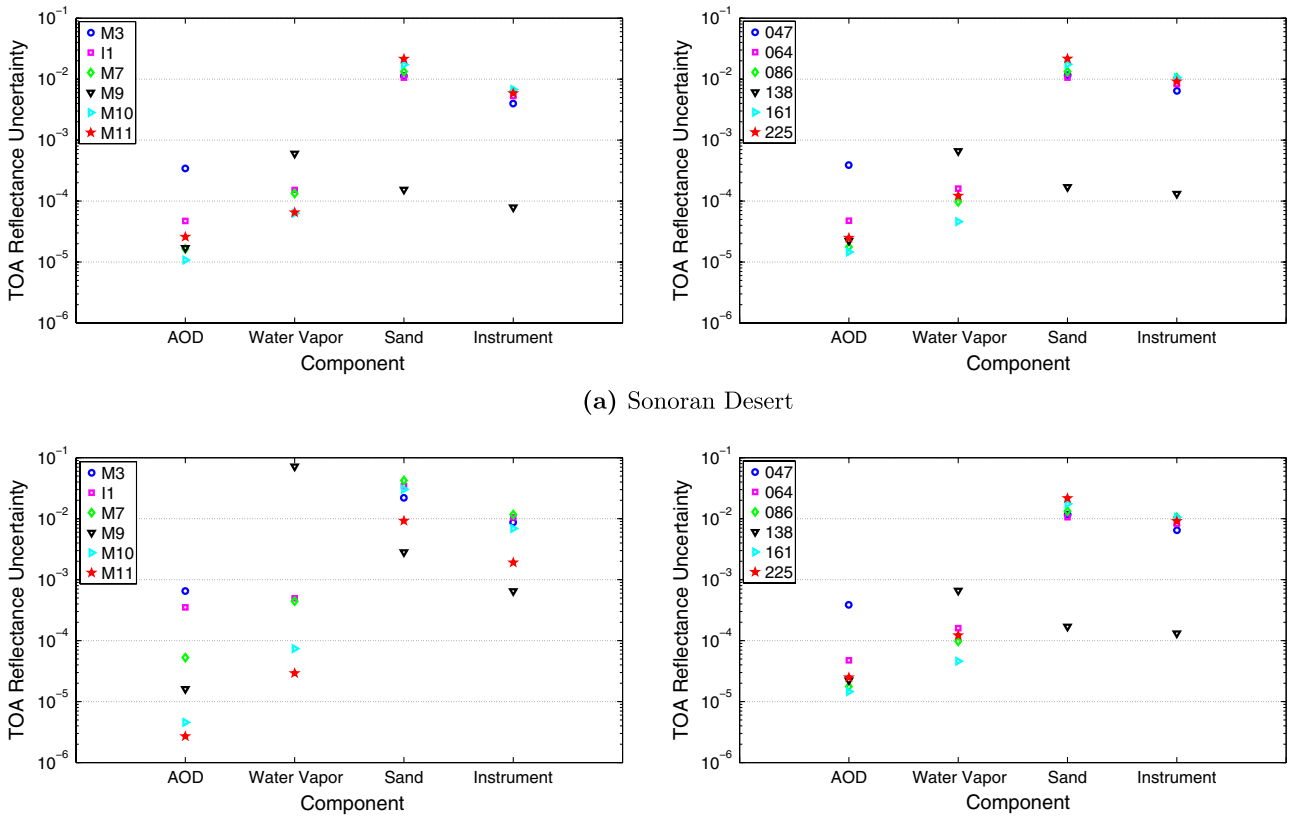

Fig. 4. TOA reflectance uncertainty contributions of VIIRS (left) and ABI (right) channels for the 6SV simulation at the (a) Sonoran Desert and (b) White Sands sites. Note that the instrument and/or target reflectance uncertainty dominate.

the Sonoran Desert site and in two ABI channels for the White Sands site (Fig. 5) by showing that the difference between the TOA reflectance generated by AVIRIS and the simulated values are lower than the ($k = 1$) uncertainty of the comparison. Validating some of the other channels was nearly successful, especially for 064, I1, 086, M7, and M9 for White Sands, as shown in Fig. 5, since the biases only slightly exceed the uncertainties. This demonstrates that, with the constraints imposed by the ground measurements and the choice of pixel according to its spatial uniformity, scientists can simulate TOA reflectance for some VIIRS and ABI channels over the Sonoran Desert and White Sands to determine radiometric biases within the stated uncertainties for these channels.

Neglected uncertainty contributions from the sand reflectance spectrum may explain the failure to validate some channels: unequal mixing between different surface types, nonrepresentative samples, and bi-directional reflectance effects. We observed the limitations of using nonrepresentative samples through our comparison of the simulation results with the most closely matched pixels from AVIRIS. These pixels represent the case of the aircraft sensor viewing only pixels that most closely correspond to the measured ground reflectance. Figure (6) shows the simulated TOA reflectance spectra (from MODTRAN) ($\rho(\lambda)$) and the measured AVIRIS TOA reflectance spectra using the most uniform pixels (AVIRIS—uniform) and using the best matched pixels (AVIRIS—matched); it also shows the effective values over the channels (generated in 6SV). This demonstrates that pixels well-matched to the simulations exist within the AVIRIS images over the Sonoran Desert and White Sands sites. In the optimal case, all these pixels would be located in the same area that AVIRIS is viewing, in an area comparable to the satellite sensor's footprint. Thus, the spatial overlap of ground sample measurement and aircraft image, as well as the uniformity of that area, determine whether the aircraft and ground measurements are compatible.

We neglected uncertainty in the radiative transfer model used in the formal uncertainty analysis presented here but compared the outputs from 6SV and MODTRAN to better understand their uncertainties. Table 3 lists their percentage differences $(\rho_{1,j,2} - \rho_{1,j,1})/\rho_{i,j,1} \times 100\%$, where a third index is added to represent 6SV(1) or MODTRAN(2). The simulations show that, using the same conditions as in Table 1, the TOA reflectance for ABI agree well, except in channel 138, where water vapor absorption is significant. We found some explanation for the slight mismatch in the other channels by repeating the simulations while substituting target reflectance of 0.0 for 1.0; the results using a reflectance of 1.0 agreed much better than for 0.0 (except in channel

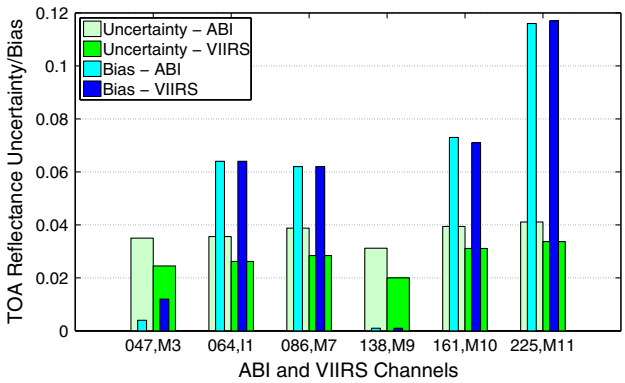

(a) Sonoran Desert

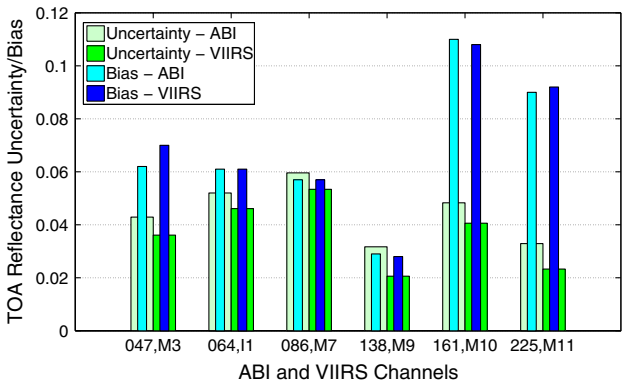

(b) White Sands

Fig. 5. Comparison of VIIRS/ABI TOA reflectances, calculated with 6SV and retrieved from the most uniform pixel-sized region of an AVIRIS image over the (a) Sonoran Desert and (b) White Sands sites. The bias is the absolute difference between the 6SV-simulated and AVIRIS-retrieved TOA reflectance values, and the uncertainty is the combined uncertainty ($k = 1$) of the comparison. A successful validation is shown by a bias of less than the uncertainty.

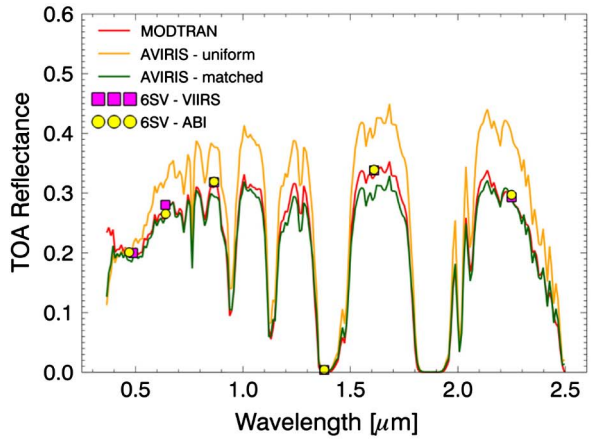

(a) Sonoran Desert

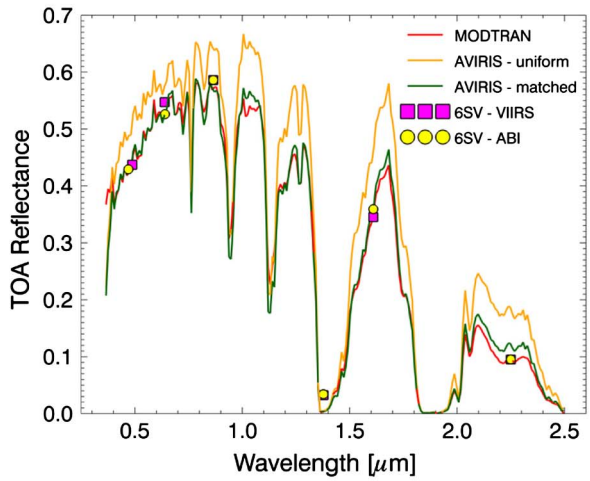

(b) White Sands

Fig. 6. ABI/VIIRS spectral and effective TOA reflectance generated using MODTRAN and 6SV, respectively. These are compared with AVIRIS pixels chosen by one of two methods: using a group of matched pixels (AVIRIS—matched) or using a uniform region of pixels (AVIRIS—uniform). The results are given over the (a) Sonoran Desert and (b) White Sands National Monument sites.

138). This result is consistent with a previous finding that scattering is handled differently in the two radiative transfer models [36], since these effects dominate in the zero-reflectance case. In setting the water vapor to 0.0 g/cm^2, we observed good agreement between the models. The agreement was poor for high water vapor (4.1 g/cm^2), suggesting that the water vapor absorption modeling has high uncertainty.

Although we roughly accounted for footprint differences between AVIRIS and ABI, we neglected

Table 3. 6SV-MODTRAN Percent Difference for ABI TOA Reflectance[a]

	ABI Channels->	047	064	086	138	161	225
Sonoran Desert	[b]Nominal conditions	0.249	1.43	−0.909	−85.7	−1.42	−1.99
White Sands	[b]Nominal conditions	0.956	2.15	−0.649	−89.7	−1.00	−0.946
	Target reflectance = 0	4.38	4.51	−9.09	−31.3	2.69	132
	Target reflectance = 1	1.11	1.97	−0.839	−91.1	−0.969	−1.05
	Water vapor = 4 g/cm^2	0.991	1.50	−1.25	−74.4	−1.75	−2.76
	Water vapor = 0	1.06	2.26	−0.549	−0.908	−0.842	−0.696

[a]Percent difference = $(\rho_{1,j,2} - \rho_{1,j,1})/\rho_{i,j,1} \times 100\%$ (first index: 1—ABI; second index—channel; third index: 1—6SV, 2—MODTRAN).

[b]Nominal conditions refer to those used in Table 1. The other conditions shown use these conditions but substitute the target reflectance for water vapor.

these differences between VIIRS and ABI in the results of Fig. 5, where the radiometric bias changed by 1% to 2% using the nominal footprints, instead of the 2 km values used for both VIIRS and ABI. So scientists need to recalculate the radiometric biases to account for the fields of view when both ABI and VIIRS are on-orbit.

In order to validate the study, we recommend repeating the simulations for an AVIRIS campaign over a highly uniform reflectance area using ground measurements in that area. Repeating the validation once both the ABI and VIIRS are on-orbit will yield more accurate biases, since they will use on-orbit geometries. We also recommend further studies to explore these effects using additional radiative transfer simulations.

4. Conclusion

We calculated radiometric biases and their uncertainties using the spectral response functions of VIIRS and ABI over calibration sites in the Sonoran Desert and White Sands National Monument, and validated some of their uncertainties using aircraft hyperspectral sensor images. We believe this helps establish measurement consistency of ABI, before GOES-R launch, with VIIRS to support numerical weather prediction and other environmental applications. Calibration engineers can also use these results to detect anomalies during future ABI-VIIRS inter-comparisons and calculate them for other geometric and atmospheric conditions using radiative transfer simulations. After GOES-R launch, the predicted biases should be modified with updated ground measurement and aircraft campaign data using ABI/VIIRS view geometries and footprints.

The authors would like to thank those who supplied data for this work: Dr. P. Campbell, T. Dickerson and S. Reckard (sample reflectance from White Sands and Sonoran Desert), J. Van Den Bosch, B. Holben, and the dedicated AERONET staff at GSFC (aerosol and water vapor from White Sands), and Dr. R. Iacovazzi (aerosol and water vapor from the Sonoran Desert). The authors also thank Dr. R. Datla, Dr. R. Kacker, and Dr. A. Smirnov for helpful discussions, and S. Esposito for his assistance with MODTRAN. This work is partially funded by GOES-R. The manuscript contents are solely the opinions of the authors and do not constitute a statement of policy, decision, or position on behalf of NOAA or the U.S. government.

References

1. T. J. Schmit, M. M. Gunshor, W. P. Menzel, J. J. Gurka, J. Li, and A. C. Bachmeier, "Introducing the next-generation advanced baseline imager on GOES-R," Bull. Am. Meteorol. Soc. **86**, 1079–1096 (2005).
2. M. Smith and D. Karlson, "The GOES-R series: the nation's next-generation geostationary operational environmental satellites," Earth Scientist **28**, 18 (2012).
3. J. C. Bremer, J. C. Criscione, M. S. Maxwell, J. A. Kronenwetter, and T. R. Pedersen, "Calibration of the solar reflective channels in an integrated operational weather satellite system in the era of NPOESS and GOES-R," Proc. SPIE **5658**, 38–48 (2005).
4. "Algorithm and Theoretical Basis Document: ABI Aerosol Detection Product," NOAA/NESDIS/STAR September 2010, http://www.goes-r.gov/resources/docs.html.
5. "GOES-R Advanced Baseline Imager (ABI) algorithm theoretical basis document for suspended matter/aerosol optical depth and aerosol size parameter," NOAA/NESDIS/STAR September 2010, http://www.goes-r.gov/resources/docs.html.
6. C. Cao, M. Weinreb, and H. Xu, "Predicting simultaneous nadir overpasses among polar-orbiting meteorological satellites for the intersatellite calibration of radiometers," J. Atmos. Ocean. Technol. **21**, 537–542 (2004).
7. L. Wang, X. Wu, Y. Li, M. Goldberg, and S. Sohn, "Comparison of AIRS and IASI radiances using GOES imagers as transfer radiometers toward climate data records," J. Appl. Meteorol. **49**, 478–492 (2010).
8. C. Cao, F. J. De Luccia, X. Xiong, R. Wolfe, and F. Weng, "Early on-orbit performance of the visible infrared imaging radiometer suite onboard the suomi national polar-orbiting partnership (S-NPP) satellite," IEEE T Geosci. Remote **0196**, 2892 (2013).
9. C. Schueler, J. E. Clement, P. E. Ardanuy, C. Welsch, F. DeLuccia, and H. Swenson, "NPOESS VIIRS sensor design overview," Proc. SPIE **4483**, 11–23 (2002).
10. S. W. Brown, G. P. Eppeldauer, and K. R. Lykke, "Facility for spectral irradiance and radiance responsivity calibrations using uniform sources (SIRCUS)," Appl. Opt. **45**, 8218–8237 (2006).
11. C. Cao, M. Weinreb, and S. Kaplan, "Verification of the HIRS spectral response functions for more accurate atmospheric sounding," presented at CALCON Technical Conference on Characterization and Radiometric Calibration for Remote Sensing, Logan, Utah, U.S., August 2004.
12. P. M. Teillet, G. Fedosejevs, K. J. Thome, and J. L. Barker, "Impacts of spectral band difference effects on radiometric cross-calibration between satellite sensors in the solar-reflective spectral domain," Remote Sens. Environ. **110**, 393–409 (2007).
13. A. P. Trishchenkoa, J. Cihlara, and Z. Lia, "Impacts of spectral band difference effects on radiometric cross-calibration between satellite sensors in the solar-reflective spectral domain," Remote Sens. Environ. **110**, 393–409 (2007).
14. M. Gunshor, T. J. Schmit, W. P. Menzel, and D. C. Tobin, "Intercalibration of broadband geostationary imagers using AIRS," J. Atmos. Ocean. Technol. **26**, 746–758 (2009).
15. L. Wang, C. Cao, and P. Ciren, "Assessing NOAA-16 HIRS radiance accuracy using simultaneous nadir overpass observations from AIRS," J. Atmos. Ocean. Technol. **24**, 1546–1561 (2007).
16. H. Cosnefroy, M. Leroy, and X. Briottet, "Selection and characterization of Saharan and Arabian desert sites for the calibration of optical satellite sensors," Remote Sens. Environ. **58**, 101–114 (1996).
17. C. R. N. Rao, C. Cao, and N. Zhang, "Inter-calibration of the moderate-resolution imaging spectroradiometer and the along track scanning radiometer-2," Int. J. Remote Sens. **24**, 1913–1924 (2003).
18. C. Nianzeng, B. G. Grant, D. E. Flittner, P. N. Slater, S. F. Biggar, R. D. Jackson, and S. M. Moran, "Results of calibrations of the NOAA-11 AVHRR made by reference to calibrated SPOT imagery at White Sands, New Mexico," Proc. SPIE **1493**, 182–194 (1991).
19. G. Chander, X. Xiong, T. Choi, and A. Angal, "Monitoring on-orbit calibration stability of the Terra/MODIS and Landsat 7 ETM+ sensors using pseudo-invariant test sites," Remote Sens. Environ. **114**, 925–939 (2010).
20. O. Dubovik, A. Smirnov, N. Holben, T. F. Eck, and I. Slutsker, "Accuracy assessments of aerosol optical properties retrieved from aerosol robotic network (AERONET) sun and sky radiance measurements," J. Geophys. Res. **105**, 9797–9806 (2000).
21. K. D. Knobelspiesse, C. Pietras, G. S. Fargion, M. Wang, R. Frouin, M. A. Miller, A. Subramaniam, and W. M. Balch, "Maritime aerosol optical thickness measured by handheld sun photometers," Remote Sens. Environ. **93**, 87–106 (2004).

22. R. O. Green, M. L. Eastwood, C. M. Sarture, T. G. Chrien, M. Aronsson, B. J. Chippendale, J. A. Faust, B. E. Pavri, C. J. Chovit, M. Solis, M. R. Olah, and O. Williams, "Imaging spectroscopy and the airborne visible/infrared imaging spectrometer (AVIRIS)," Remote Sens. Environ. **65**, 227–248 (1998).
23. https://cs.star.nesdis.noaa.gov/GOESRCWG/PublicData.
24. https://cs.star.nesdis.noaa.gov/NCC/SpectralResponseVIIRS.
25. S. Y. Kotchenova, E. F. Vermote, R. Matarrese, and F. J. Klemm, Jr., "Validation of a vector version of the 6S radiative transfer code for atmospheric correction of satellite data. Part I: path radiance," Appl. Opt. **45**, 6762–6774 (2006).
26. A. Berk, L. S. Bernstein, and D. C. Robertson, "MODTRAN: a moderate resolution model for LOWTRAN 7," Scientific report, Spectral Sciences, Inc. (1987).
27. A. Berk, G. P. Anderson, P. K. Acharya, L. S. Bernstein, L. Muratov, J. Lee, M. Fox, S. M. Adler-Golden, J. H. Chetwynd, M. L. Hoke, R. B. Lockwood, J. A. Gardner, T. W. Cooley, C. C. Borel, P. E. Lewis, and E. P. Shettle, "MODTRAN5: 2006 update," Proc. SPIE **6233**, 62331F (2006).
28. G. Thuillier, M. Herse, D. Labs, T. Foujols, W. Peetermans, D. Gillotay, P. C. Simon, and H. Mandel, "The solar spectral irradiance from 200 to 2400 nm as measured by the SOLSPEC spectrometer from the atlas and Eureca mission," Sol. Phys. **214**, 1–22 (2003).
29. F. A. Kruse, A. B. Lefkoff, J. W. Boardman, K. B. Heidebrecht, A. T. Shapiro, P. J. Barloon, and A. F. H. Goetz, "The spectral image processing system (SIPS)—interactive visualization and analysis of imaging spectrometer data," Remote Sens. Environ. **44**, 145–163 (1993).
30. "GUM 1995 with minor Corrections: Evaluation of measurement data—Guide to the expression of uncertainty in measurement," BIPM, IEC, IFCC, ILAC, ISO, IUPAC, IUPAP, OIML, 2008, http://www.bipm.org/en/publications/guides/gum.html.
31. A. Pearlman, Earth Resources Technology, 5825 University Research Ct. Suite 3250, College Park Maryland 20740, USA, R. Datla, R. Kacker, and C. Cao are preparing a manuscript to be called "Translating radiometric requirements for satellite sensors to match international standards."
32. R. Kacker, K. Sommer, and R. Kessel, "Evolution of modern approaches to express uncertainty in measurement," Metrologia **44**, 513 (2007).
33. "GOES-R Series Mission Requirements Document (MRD)," P417-R-MRD-0070, August 2011, http://www.goes-r.gov/syseng/docs/MRDv314.pdf.
34. N. Baker, "Joint Polar Satellite System (JPSS) VIIRS radiometric calibration Algorithm Theoretical Basis Document ATBD," Goddard Space Flight Center 2012, http://npp.gsfc.nasa.gov/science/documents.html.
35. J. L. Gardner, "Uncertainties in interpolated spectral data," J. Res. Natl. Inst. Stan. **108**, 69–78 (2003).
36. F. Callieco and F. Dell'Acqua, "A comparison between two radiative transfer models for atmospheric correction over a wide range of wavelengths," Int. J. Remote Sens. **32**, 1357–1370 (2011).